https://doi.org/10.5194/egusphere-2026-4769
Preprint. Discussion started: 14 September 2026

The 2022 AQUAS–Tsukuba campaign: Part I. OH reactivity analysis and NO-corrected reactivity ratios for improved ozone regime evaluation

Jiaru Li[1,2], Yosuke Sakamoto[2], Yu Morino[2], Kei Sato[2], Koichi Egami[3], Nanase Kohno[4], Yasuhiro Sadanaga[5], Shungo Kato[6], Yoshihiro Nakashima[7], Ayako Yoshino[2], Akinori Takami[2], Yugo Kanaya[1], Yoshizumi Kajii[8]

[1]Japan Agency for Marine-Earth Science and Technology, Kanagawa, 236-0001, Japan
[2]National Institute for Environmental Studies, Tsukuba, 305-8506, Japan
[3]Graduate School of Human and Environmental Studies, Kyoto University, Kyoto, 606-8501, Japan
[4]Department of Science, Kindai University, Osaka, 577-8502, Japan
[5]Department of Applied Chemistry, Graduate School of Engineering, Osaka Metropolitan University, Osaka, 599-8531, Japan
[6]Graduate School of Urban Environmental Sciences, Tokyo Metropolitan University, Tokyo 192-0397, Japan
[7]Department of Environmental Science on Biosphere, Graduate School of Agriculture, Tokyo University of Agriculture and Technology, Tokyo, 183-8509, Japan
[8]School of Environmental Science and Engineering, Qingdao University, Qingdao, 266071, PR China

Correspondence to: Jiaru Li (jiaru.li@jamstec.go.jp) and Yosuke Sakamoto (sakamoto.yosuke@nies.go.jp)

Abstract.

Revisiting an intensive field campaign is important for assessing the influences of human activity and natural event on on-site air quality. We conducted observations in Tsukuba, Japan, during the summer of 2022 at the same site as the 2017 AQUAS–Tsukuba summer campaign, enabling a comparison of OH reactivity and related trace species after a lustrum. The combined WRF-CMAQ model simulations provided supplementary speciation of the OH reactivity, enabling extrapolation to unmeasured trace gases. Substantial reductions in anthropogenic emissions over the five years reduced the average total OH reactivity from 12.9 s^{-1} to 6.0 s^{-1}. However, total OH reactivity was not fully explained by the concurrently measured trace species or model simulations, and at least 35% remained unidentified in both campaigns. High total OH reactivity and observation-based missing OH reactivity were associated with high wind speeds that brought air pollutants from the Tokyo metropolitan area. The model showed bias in the spatiotemporal variations of meteorological conditions and trace species, with large underestimation at noon when the air influx was from a pristine site, and from afternoon to midnight when the air influx was from a polluted site. A constrained model simulation that combined 2017 emission inventories (except biogenic emissions) with 2022 meteorological conditions quantified the significance of primary emissions' contributions to the 2022 campaign. Additionally, we propose evaluating the ozone regime via using $\frac{k_{VOC}}{k_{NOx}} = 28.9 \cdot [NO]$ (NO in ppbv), which reduces the overestimation of the VOC-limited regime under low NO conditions and supports for ozone mitigation strategies.

https://doi.org/10.5194/egusphere-2026-4769
Preprint. Discussion started: 14 September 2026

1 Introduction

Assessing the science related to climate change and air pollution requires an understanding of the loading of short-lived trace species (Calvin et al., 2023). Top-down OH reactivity measurements, which quantify the total loading of active trace species, are an efficient approach for interpreting on-site air quality. However, current measurements of OH reactivity are limited and require expensive, hard-to-manage instruments, making long-term observations extremely challenging and costly. In contrast, bottom-up OH reactivity estimation, typically sums the decay rates of individual OH reactants from measurements and cannot always reconcile with top-down results in complex ambient environments. Model simulations predict short-lived trace species from emissions, reactions, and specific meteorological conditions, which usually helps bridge the gap between top-down and bottom-up approaches and explore unknown OH reactants. These three approaches are essential for fully understanding atmospheric chemical transformations and for assessing oxidation capacity at local or regional scales.

Field-based top-down OH reactivity measurements have been conducted worldwide over the past decades using either direct methods, such as the pump-probe technique (Hansen et al., 2014; Kovacs and Brune, 2001; Lee et al., 2009; Lou et al., 2010; Parker et al., 2011; Sadanaga et al., 2004a), or indirect methods, such as the comparative reactivity method (CRM) (Sinha et al., 2008, 2012). An intercomparison of the two methods in an urban environment found good agreement for NOx concentrations below 40 ppbv, whereas the CRM in an NOx-rich case exhibited artifacts from HO_2+NO reactions (Hansen et al., 2015). An improved CRM successfully reduced ambient NO interference by continuously inducing NO in the system, thereby reducing HO_2 (Wang et al., 2021). Field observations have covered ambient conditions in urban, suburban, forest, coastal, marine, and aerial areas (Chatani et al., 2009; Kovacs et al., 2003; Li et al., 2021; Mao et al., 2009; Ramasamy et al., 2018; Whalley et al., 2016; Yang et al., 2016; Yoshino et al., 2012). The campaigns conducted at anthropogenic emission-dominated sites showed similar diurnal trends but at different magnitudes, with a peak in the early morning, a drop at noon, and a slight increase in the late afternoon to evening, capturing the important contributions of NOx emissions during rush hours (Yang, 2023).

Nevertheless, unexplained OH reactivity in either bottom-up measurements or model simulations is known as missing OH reactivity. Both the bottom-up approach and model simulation contain biases due to kinetic rate constants, unconsidered chemical mechanisms, physical processes, and potential instrument uncertainties or model limitations. Previous field campaigns have reported 30–50% missing OH reactivity in summer at polluted/semi-polluted sites (Yang et al., 2016). The seasonality of missing OH reactivity has been reported to increase from the cold to the warm seasons (Brune et al., 2022; Yoshino et al., 2012). In addition, the 3-D air quality model (WRF-CMAQ) simulated OH reactivity in Tokyo, which was significantly underestimated owing to VOC bias. To bridge this gap, researchers have applied scaling factors for each trace species, derived from the measurements, to account for the remaining 40% of the missing OH reactivity (Chatani et al., 2009).

https://doi.org/10.5194/egusphere-2026-4769
Preprint. Discussion started: 14 September 2026

On-site field campaigns can provide temporary investigations at short spatial scales, but routine field campaigns at the same site are currently scarce for understanding chemical transformations over long timescales. With ongoing air regulations, we expect improvements in air quality. The scientific questions remain regarding the extent to which anthropogenic air pollutants have been reduced, how many unknown air mixing ratios remain, and how to further evaluate their oxidation capacity. Previously, multiple campaigns (TexAQS2000, TRAMP2006, and SHARP2009) in Houston were conducted over different summer years, observing a similar diurnal ozone production regime that transitioned from VOC-limited to NOx-limited at noon (Mao et al., 2010; Ren et al., 2013). They reported that the NOx reduction sustained longer NOx-limited conditions in SHARP2009. A detailed comparison of same-site campaigns would be meaningful for diagnosing the influence of emission reductions from meteorological dispersive and transportive effects. We conducted an intensive field campaign during the summer of 2022 at the same site as the 2017 Tsukuba summer campaign (Li et al., 2020). Although each campaign entailed only two weeks of observations, we believe that the short-term snapshot could capture the long-term evolution through interpretation of the WRF-CMAQ simulation. To confirm the interaction between meteorology and emissions, an extra-constrained scenario using 2017 emission inventories and 2022 meteorology provides more explicit comparisons. Such cross-comparisons should provide insights into ozone mitigation strategies to uncover the effects of pollutant regulation in a changing society.

2 Method

2.1 Site description

The summer campaign was conducted from 22 August to 4 September 2022, at the National Institute for Environmental Studies (NIES; 36°03′N, 140°07′E) in Tsukuba, Japan, a suburban site located northeast of the Tokyo metropolitan area. The measurements were performed at the same site as in the 2017 AQUAS–Tsukuba summer campaign reported by Li et al. (2020). The site is characterized by a humid continental climate and influenced by both anthropogenic and biogenic emissions owing to its proximity to the Tokyo metropolitan area, Mt. Tsukuba and Lake Kasumigaura. During the campaign, the hourly air temperature ranged from 19 to 34 °C, comparable to that observed during the 2017 campaign. Table 1 summarizes the suite of instruments used to measure the meteorological parameters, actinic fluxes, inorganic trace species, VOCs, oxygenated VOCs, XO_2 radical ($XO_2 \equiv HO_2 + RO_2$), and total OH reactivity.

2.2 Measurement of total OH reactivity

Total OH reactivity was measured using a laser pump and laser-induced fluorescence (LP-LIF) technique (Sadanaga et al., 2004a). The instrument was deployed at the ground level, and detailed descriptions of the measurement principle and field applications are available elsewhere (Kohno et al., 2022; Li et al., 2020, 2021, 2022; Ramasamy et al., 2016, 2018; Sadanaga et al., 2004a; Yoshino et al., 2006, 2012). Therefore, only a brief description is provided here.

https://doi.org/10.5194/egusphere-2026-4769
Preprint. Discussion started: 14 September 2026

The LP-LIF instrument comprises two parallel cells: a reaction cell and a laser-induced fluorescence (LIF) cell. In the reaction cell, a pump laser (Nd:YAG system, Tempest 300, New Wave Research) photolyzed ozone (typically >80 ppbv in the reaction cell) to generate OH radicals. Ozone was generated by photolysis of oxygen under Hg lamp irradiation (185 nm), and was supplemented with ambient ozone introduced from the sampled air. The LIF cell was connected to the reaction cell through a 0.5-mm-diameter orifice. OH radicals were excited in situ by a probe laser via the $Q_1(2)$ $A_2(v'=0) \leftarrow X_2(v''=0)$ transition, and the resulting fluorescence was detected with a photomultiplier tube (PMT; R2256P, Hamamatsu). The PMT was gated off during each laser pulse to prevent detector saturation and enable accurate fluorescence photon counting.

Zero-air measurements were routinely performed once a day at various times using a zero-gas generator (Thermo Scientific Model 111) that supplied air containing only nitrogen and oxygen. No significant day-to-day variations were observed in the instrumental background. The average daily baseline, primarily attributed to thermal OH diffusion from the laser photolysis region, was 3.7 ± 0.2 s^{-1}, corresponding to an instrumental uncertainty of approximately 5%. Ambient air was sampled through a 20 m, 1/2-inch perfluoroalkoxy (PFA) tube at a flow rate of 13 standard liters per minute (SLM; 273K and 1 atm). The residence time in the sampling line was approximately 9 s, which is sufficiently short to neglect chemical losses due to rapid oxidation reactions. Ambient OH reactivity (k_{OH}) was obtained by subtracting the daily background from the measured decay rate. The OH decay profiles were averaged over 240 laser shots at a repetition rate of 2 Hz, yielding a temporal resolution of 2 min. The instrument was calibrated after the field campaign using a certified propene/N_2 cylinder gas (40.4 ppmv; Sumimoto Seika Chemicals). The measured OH reactivity was corrected by using a calibration factor of 0.974. Details of the calibration procedure are shown in Fig. S1 of the Supplement.

2.3 Measurement of XO_2 concentration

The concentration of XO_2 was measured using the peroxy radical chemical amplification (PERCA) technique (Cantrell and Stedman, 1982). PERCA converts HO_2 and RO_2 radicals into NO_2 through a chain-amplification mechanism, enabling the quantification of XO_2 concentrations using a cavity-attenuated-phase-shift (CAPS) NO_2 monitor. The instrument was installed on the rooftop of an eight-story building, approximately 30 m above ground level, and collocated with a radiometer. The measurement system periodically introduced CO and NO into the reactor to convert HO_2 and most of the RO_2 radicals into NO_2. The instrument was configured as described by Sadanaga et al. (2004b).

The PERCA-CAPS system was calibrated by generating a known concentration of HO_2 radicals through the photolysis of water vapor at 185 nm using a mercury lamp in the presence of excess CO. The dependence of the chain length on RH was also characterized using the same calibration system to correct for the effect of water vapor under ambient conditions. The measurement uncertainty was estimated from the uncertainty in the generated HO_2 concentration during the calibration experiments, which was primarily associated with the absorption cross sections of O_2 and H_2O. The overall uncertainty of the system was estimated at up to 40%, reflecting variations in the calibration configuration. A detailed description of the

https://doi.org/10.5194/egusphere-2026-4769
Preprint. Discussion started: 14 September 2026

instrument and calibration of the chain length is provided by Sakamoto et al. (2026), and the corresponding calibration results are presented in the Supplement, including Fig. S2.

2.4 Ancillary Measurements

The NOx, CO, O_3, and HCHO concentrations were measured using commercial analyzers (Table 1). Except for CO, which was measured on the sixth floor of the building, all the trace gases were sampled at ground level. Details of the calibration procedures are described in the Supplement (including Fig. S3).

The VOCs were continuously measured using proton-transfer-reaction time-of-flight mass spectrometry (PTR-ToF-MS; IONICON 6000) and gas chromatography using a flame ionization detector (GC-FID; Agilent 6890). To validate the online measurements, 20 whole-air canister samples were collected twice or thrice daily during the campaign. The canister samples were subsequently analyzed by GC-FID for VOCs and by a reduction gas detector (RGD; SRI Instruments Europe GmbH) for H_2 and CO. Figure S4 compares the concentrations of representative VOCs measured using the online and offline techniques. Online VOC measurements were evaluated against canister analyses, and only validated VOC species were included in the subsequent analyses. Table S1 lists the validated VOC species, along with their average concentrations and corresponding rate coefficients for reactions with OH used in the OH reactivity calculations.

$$k'_{cal} = \sum_i k_i [X_i] \quad (1)$$

The calculated OH reactivity was obtained by summing the products of the measured concentrations ($[X_i]$) of all the validated trace species and their corresponding second-order rate coefficients with OH (k_i), as shown in Eq. (1). Rate coefficients were adopted from Li et al. (2022). Meteorological parameters, including wind speed, wind direction, RH, and atmospheric pressure, were obtained from a nearby environmental monitoring station (Fig. 1). The time series of precipitation, RH and wind speed are presented in Fig. S5.

Table 1. Information on the instrumentation for the detected objects.

Object	Technique	Time resolution	Relative uncertainty (1σ)	Note
Total OH reactivity	LP-LIF, custom-based	2-min	5%	
XO_2 concentration	PERCA-CAPS, custom-based	10-min	40%	Refer to Sakamoto et al. (2026)
NO_2	CAPS, Aerodyne	1-s	<1%	

https://doi.org/10.5194/egusphere-2026-4769
Preprint. Discussion started: 14 September 2026

NO	Chemiluminescence, Thermo 42i-TL	1-min	1%
O_3	UV-vis absorption, Dylec 1150	10-s	0.5%
CO	NDIR, Thermo 48i-TLE; RGD, SRI	1-min; offline	1%; 8%
H_2	RGD, SRI	offline	8%
VOCs	PTR-ToF-MS, IONICON 6000; GC-FID, Agilent 6890	1-min; 1-h	<1%; 9%
HCHO	Hantzsch Reaction, Aero-Laser AL4021	90-s	2%
Photolysis rate	Radiometer		
RH, temperature, humidity, wind speed, wind direction, and pressure	NIES Air Quality Research Station	1-h	

2.5 WRF-CMAQ simulations

The basic framework of the simulations was the same as that of Morino et al. (2023). Meteorological and chemical simulations were performed using the Weather Research and Forecasting (WRF) model v4.1.5 coupled with the Community Multiscale Air Quality (CMAQ) model v5.3.2. The gas-phase chemistry and aerosol processes were represented using the SAPRC07 chemical mechanism and AERO7i aerosol module, respectively. The meteorological initial and boundary conditions were obtained from the National Centers for Environmental Prediction Final (NCEP-FNL ds 083.3) operational analyses, while the chemical initial was provided by the CHASER global chemical transport model. Model outputs with a horizontal resolution of 5 km were used for all the analyses presented in this study. In addition, we used the 10-m wind speed and 10-m wind direction from the Meteorology-Chemistry Interface Processor output for spatiotemporal variations of the modeled trace species.

Three simulation scenarios were designed to investigate the relative contributions of changes in emissions and meteorological variability (Table 2). The two scenarios reproduced the atmospheric conditions during the 2017 and 2022 field campaigns using the corresponding meteorological fields and emission inventories. As part of the 2022 emissions inventory was unavailable, missing emissions were replaced with those from the most recent available inventory. In addition, a constrained scenario (M2022E2017) was simulated by combining the 2022 meteorological conditions with the 2017 anthropogenic emissions to isolate the influence of meteorological variability. The BVOC emissions were retained from the 2022 simulation

https://doi.org/10.5194/egusphere-2026-4769
Preprint. Discussion started: 14 September 2026

because they are strongly dependent on meteorological conditions, particularly temperature. Comparisons between the modeled and observed concentrations were used to evaluate the model performance and identify potential sources of uncertainty. Furthermore, the constrained simulation enabled the determination of the relative contributions of emission changes associated with air quality regulations and interannual meteorological variability to be distinguished.

Table 2. Details of the WRF-CMAQ model used in the Tsukuba field campaign over 2017 and 2022.

Source	Data	2017	2022	M2022E2017
Anthropogenic (Japan, Motor vehicles)	MOEJ	2017	2021	2017
Anthropogenic + open burning (Japan, others)	J-STREAM	2017	2021	2017
Anthropogenic (foreign)	REAS v3.2.1	2017	2020	2017
Anthropogenic (Russia)	EDGARv5.0	2017	2018	2017
Ships (Japan)	GLIMMS-AQ	2017	2020	2017
Ships (foreign)	EDGARv5.0	2017	2018	2017
Biomass burning (foreign)	GFED v4.1s	2017	2022	2017
Biogenic VOC	MEGAN v2.10	2017	2022	2022
Volcano (Japan)	JMA	2017	2022	2017
Volcano (foreign)	Carn et al. (2017)	2017	2022	2017

3 Results and discussion

3.1 Meteorological conditions during the 2022 field campaign

The meteorological conditions during the 2022 field campaign, including wind speed, air temperature, and RH, are shown in the upper panel of Fig. 1. Both the 2017 and 2022 campaigns were conducted during the late summer, and the observed temperature ranges were comparable. In 2022, the RH was generally higher when winds originated from the east-to-north sectors and decreased around midday as air temperature increased. Higher temperatures and stronger winds were associated with southern air masses, with peak wind speeds occurring in the late afternoon.

Compared with the 2017 campaign, wind speeds in 2022 were generally higher across most wind directions. The average wind speed increased by 0.57 m s^{-1}, while easterly winds exhibited similar strengths during both campaigns (lower panel of Fig. 1). The most pronounced difference was observed for nighttime winds from the south to west, where the average wind speed increased by 0.77 m s^{-1} in 2022, indicating enhanced transport of urban air masses from the Tokyo metropolitan area. In contrast, daytime easterly winds, which are associated with the lake breeze, were slightly weaker in 2022 than in 2017.

https://doi.org/10.5194/egusphere-2026-4769
Preprint. Discussion started: 14 September 2026

Overall, the meteorological conditions during the 2022 campaign favored a more efficient transport of polluted air masses from the upwind megacity region. This enhanced transport likely offset, at least in part, the reduction in local anthropogenic emissions when the two campaigns were compared.

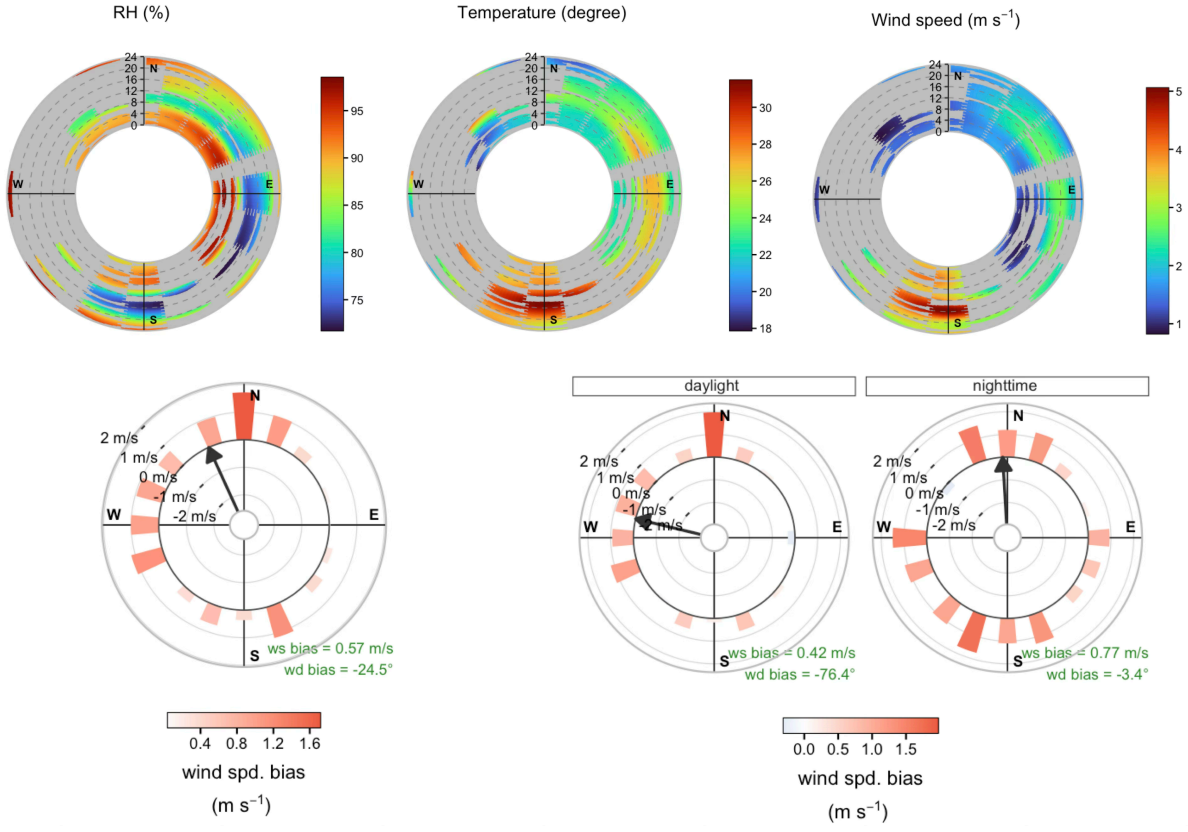

Figure 1. Upper panel: Diurnal variations of meteorological conditions, including RH, temperature, and wind speed, in the 2022 field campaign. The radial axis shows hour of the day. Lower panel: The wind condition difference regarding each wind direction from Aug 21st to 28th, 2022, compared to the same period in 2017 (left), and the results during the daytime (middle) and nighttime (right). The arrows indicate changes in the general wind direction, which comes from the West during the daytime and the North during the nighttime in 2022.

3.2 Observations during the 2022 campaign and comparison with the 2017 campaign

The time series of the measured total OH reactivity and contributions from the individual groups of OH reactants are shown in Fig. 2. The hourly mean total OH reactivity ranged from 1.9 to 16.8 s^{-1}, while the 2-min observations spanned a wider range of 1.3– 41.5 s^{-1} (Fig. S6). NOx and CO were the dominant contributors, accounting for approximately 32% of the total OH reactivity. Despite measuring more than 47 reactive trace species, 44% of the total OH reactivity remained unexplained. Based

https://doi.org/10.5194/egusphere-2026-4769
Preprint. Discussion started: 14 September 2026

on their typical background concentrations (2 ppmv for CH_4 and 700 ppbv for H_2), methane and hydrogen were estimated to contribute an additional 5.2% and 1.9%, respectively.

The backward-trajectory analysis in Fig. S7 indicated that the three largest total OH reactivity episodes (26, 27, and 31 August) occurred when air masses originated from the south and passed over the Tokyo metropolitan area before reaching the observation site. In contrast, the lowest daytime total OH reactivity was observed on 28 August, when northerly winds (Fig. 3) and precipitation (Fig. S5) promoted cleaner atmospheric conditions. Nevertheless, a substantial fraction of unidentified OH reactants was consistently observed, with particularly high contributions in the early morning and late afternoon, particularly on days with elevated total OH reactivity.

A detailed description of the 2017 Tsukuba campaign is provided by Li et al. (2020). For comparison, the modeled time series and source contributions to OH reactivity during the 2017 campaign are presented in Fig. S8 and Fig. S9, respectively. During the 2017 campaign, observations indicated that approximately 35% of total OH reactivity was unexplained, whereas the WRF-CMAQ simulation underestimated the total OH reactivity substantially, leaving approximately 68% unexplained due to underestimation of NOx, CO, and VOC concentrations.

To compare the atmospheric composition between the two campaigns, Table 3 summarizes the daytime average concentrations (mean $\pm 1\sigma$) of inorganic species, HCHO, total OH reactivity, and calculated OH reactivity, while the corresponding averages over the entire observation period are provided in Table S2. Between 2017 and 2022, daytime NOx concentration decreased by over 60%, whereas CO concentrations declined by over 30%, suggesting a smaller reduction in CO emissions than in NOx, consistent with the continued importance of residential combustion sources and their influence on atmospheric oxidation capacity (Wei et al., 2023; Zheng et al., 2018). Daytime O_3 decreased by 28%, while the reduction in campaign-average O_3 concentration was only 9%, reflecting the weak NO titration at night. Overall, indicators of primary emissions and secondary oxygenated products, represented by HCHO and calculated OH reactivity, decreased by over 54%. In contrast, O_3 exhibited a much smaller decline, suggesting that long-term changes in precursor emissions may have altered the ozone production regime. These contrasting changes in precursor concentrations and ozone also motivate the following analysis of the factors controlling OH reactivity and atmospheric oxidation capacity.

https://doi.org/10.5194/egusphere-2026-4769
Preprint. Discussion started: 14 September 2026

Table 3. Comparison of the typical "trace species", total OH reactivity, and calculated OH reactivity from hourly daytime results (6:00–18:00, not including 18:00) in 2017 and 2022. The values represent the mean ± 1σ standard deviation.

		NO	NO_2	O_3	CO	HCHO	k'_{total}	k'_{cal}	k'_{mdl}
		ppbv					s^{-1}		
Observation	2017	1.3±3.3	10.2±4.9	42.2±21.4	309±83	3.9±1.8	13.1±4.8	8.1±3.2	
	2022	0.24±0.34	4.0±1.9	30.3±10.4	217±43	1.8±1.3	6.8±2.4	3.7±1.1	
WRF-CMAQ	2017*	0.67±0.90	3.2±2.9	54.2±14.7	119±27	2.4±1.0			5.1±2.5
	2022#	0.79±1.0	3.3±2.2	42.1±18.4	112±32	1.2±0.5			3.0±1.0
	M2022E2017#	0.89±1.1	4.2±2.8	45.1±18.1	139±37	1.4±0.6			3.7±1.3

*2017 simulation results from 21 to 28 August, which is the same as the OH reactivity measurement period. The average daytime simulated OH reactivity was 3.7 ± 2.0 s^{-1} during the period of 20 August to 5 September. The time-series results are shown in Fig. S8.

#2022 simulation results from 24 August to 4 September, which is the same as the OH reactivity measurement period.

https://doi.org/10.5194/egusphere-2026-4769
Preprint. Discussion started: 14 September 2026

245

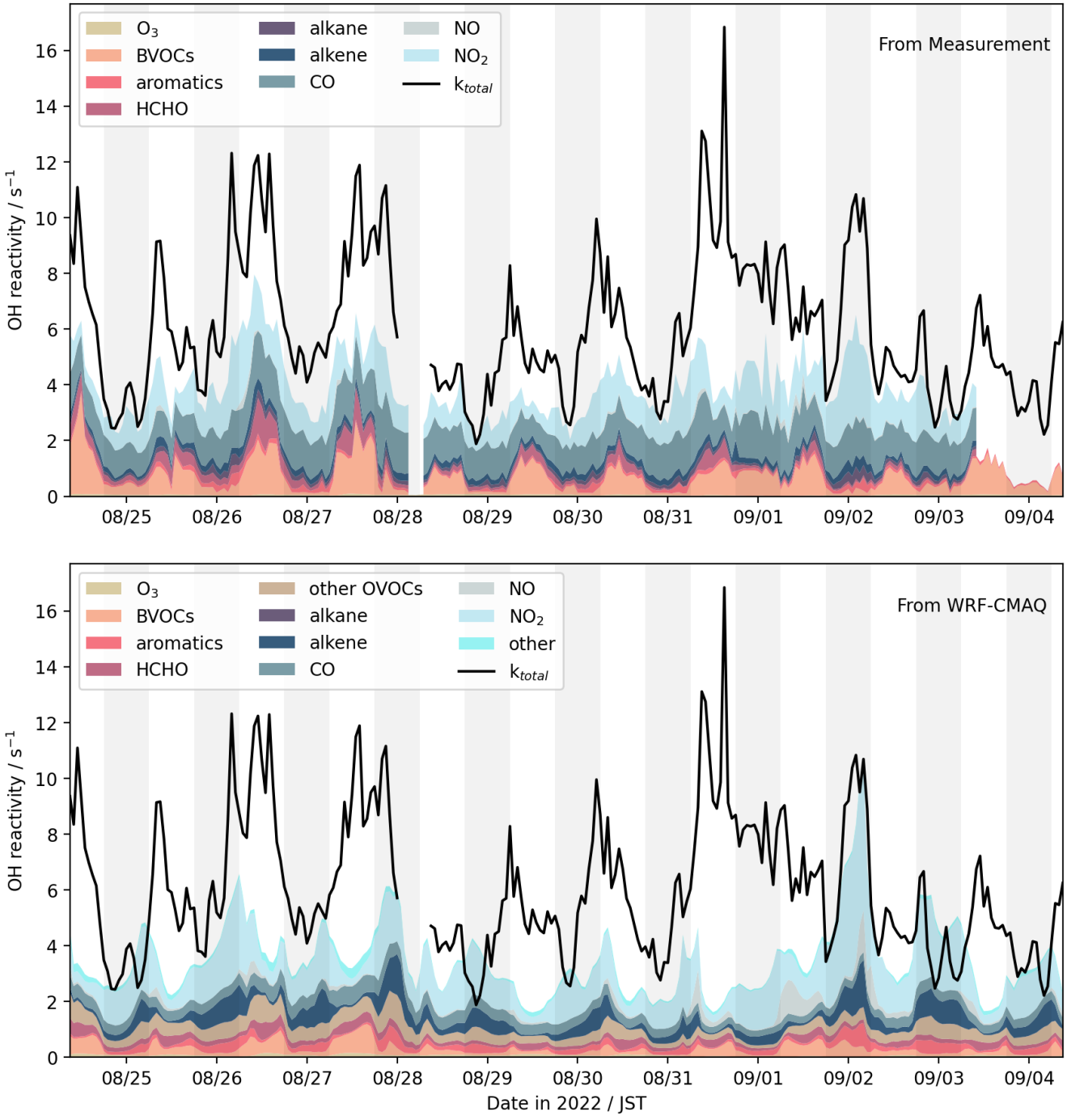

Figure 2. **Hourly average of total OH reactivity (in lines) and its contribution from each group of trace species (in stocked areas) based on measurements (upper panel) and simulations (bottom panel).**

https://doi.org/10.5194/egusphere-2026-4769
Preprint. Discussion started: 14 September 2026

3.3 Source characteristics of total and missing OH reactivity

Stronger winds during the 2022 campaign enhanced the transport of air pollutants from upwind source regions, despite reduced local emissions. To investigate the dominant source characteristics of these air pollutants, the total OH reactivity, calculated OH reactivity, and modeled OH reactivity were analyzed as functions of wind speed and wind direction (Fig. 3). By 2022, the highest total OH reactivity was associated with strong southerly winds, indicating the transport of polluted air masses from the Tokyo metropolitan area. By contrast, applying the same analysis to the 2017 campaign (Fig. S10) showed that the highest total OH reactivity occurred predominantly under relatively stagnant conditions, suggesting a stronger influence of local emissions.

Although the observations revealed distinct source characteristics for the two campaigns, neither the measured trace species nor the WRF-CMAQ simulations fully reproduced the magnitude or spatial distribution of the total OH reactivity. This discrepancy highlights unidentified OH-reactive species in the observations, as well as uncertainties in the model's representation of meteorological processes and chemical interactions. During the 2017 campaign, the calculated OH reactivity captured the southwest–northeast gradient of the total OH reactivity reasonably well (Fig. S10). In contrast, the 2022 campaign exhibited increased contributions from secondary products and biogenic VOCs under easterly and southerly winds, resulting in distinct spatial distributions of the calculated OH reactivity. The model simulations for both campaigns primarily reflected the dilution effect, predicting a higher OH reactivity under weaker wind conditions.

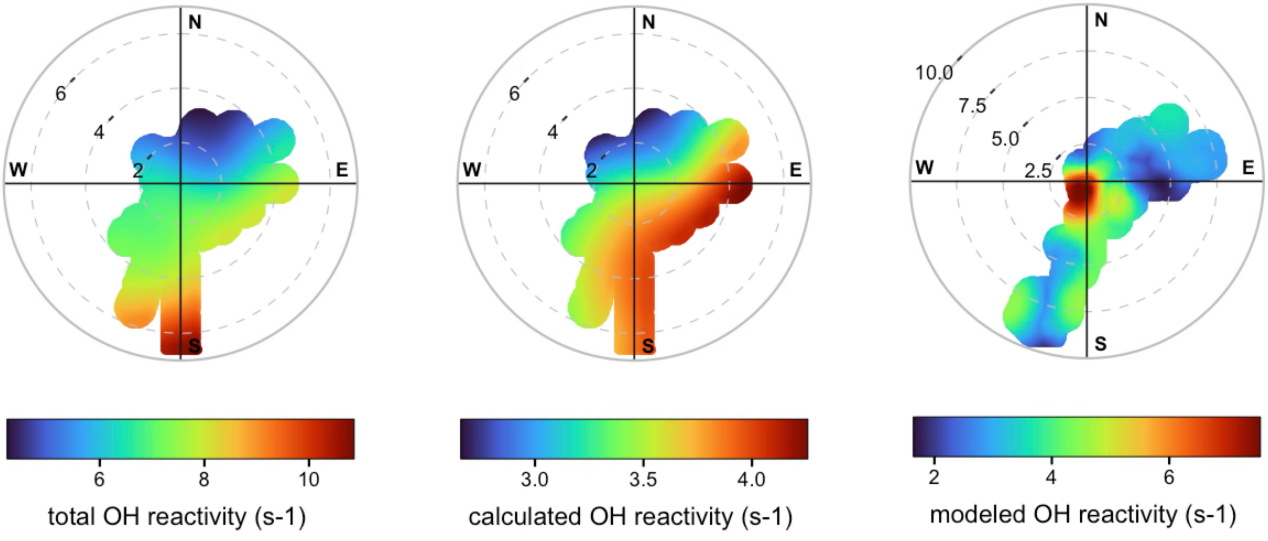

Figure 3. Bivariate polar plot of total OH reactivity (left), calculated OH reactivity from measured trace species (middle), and modeled OH reactivity (right) in 2022. The radial axis shows the wind speed in m s^{-1}. The monitored surface wind speed and direction were used for the left and middle panels, whereas the model-output wind speed and direction at 10 m were used for the right panel.

https://doi.org/10.5194/egusphere-2026-4769
Preprint. Discussion started: 14 September 2026

The spatial distributions of the missing OH reactivity derived from observations and the model are shown in Fig. 4. In 2022, the observation-based missing OH reactivity was largest under strong southerly winds, suggesting substantial contributions from transported primary emissions and their oxidation products originating from the Tokyo metropolitan area. The missing OH reactivity decreased progressively as wind speeds weakened. The model reproduced the elevated missing OH reactivity under southerly flow to some extent but additionally exhibited high missing OH reactivity under moderate southeasterly winds. This discrepancy is likely due to biases in the simulated meteorological fields, which also appeared to have stronger winds than those monitored in both years. For example, the model underestimated up to 64% of the BVOCs. In addition to underrated biogenic sources, meteorological bias in the model contributes to the underestimation by altering BVOC lifetimes. Previously, a scaling factor of approximately 4 was applied to isoprene to reduce this discrepancy (Chatani et al., 2009). This treatment exhibited consistency and inconsistency on a daily scale, indicating meteorological influence. The diurnal variations in the missing OH reactivity (Fig. S11) provided further insight into its origin. In 2022, both the observation-based and model-derived missing OH reactivity exhibited enhanced values around noon under northeasterly winds, indicating additional contributions from secondary oxidation products formed during daytime photochemistry. In contrast, the elevated missing OH reactivity associated with the southerly winds persisted throughout the day, supporting the interpretation that unidentified reactive species were continuously transported from the Tokyo metropolitan area. Overall, the WRF-CMAQ model underestimated the total OH reactivity due to primary emissions, secondary products and meteorological fields.

Compared with 2022, the source characteristics during the 2017 campaign were less distinct due to weaker meteorological forcing (lower panel in Fig. 4 and Fig. S11). The highest missing OH reactivity occurred around midday under westerly to northerly winds. Although the observed and modeled spatial patterns were generally similar, the model consistently predicted a larger missing OH reactivity than that inferred from the observations. Together, these results suggest that anthropogenic emission controls substantially reduced the overall burden of reactive air pollutants between 2017 and 2022, while the meteorological conditions during the 2022 campaign favored the regional transport of urban air masses, partially compensating for the reduction in local emissions.

https://doi.org/10.5194/egusphere-2026-4769
Preprint. Discussion started: 14 September 2026

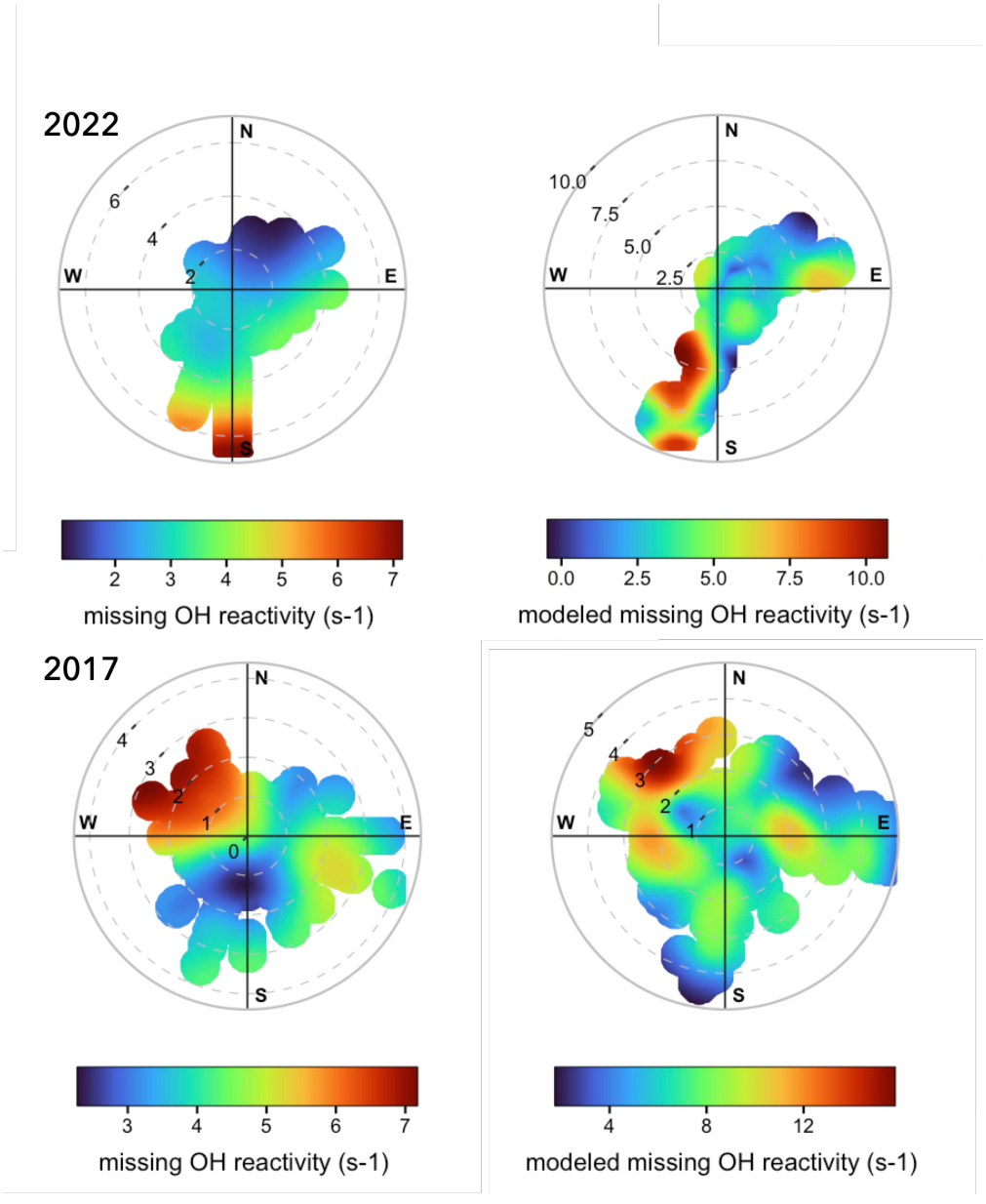

Figure 4. **Bivariate polar plot of missing OH reactivitiy from measurements (left panel) and model simulations (right panel) in 2022 (upper panel) and 2017 (lower panel). The radial axis shows the wind speed in m s^{-1}. For the left panel, the monitored surface wind speed and wind direction were used; for the right panel, the model output of 10-m wind speed and direction was used.**

https://doi.org/10.5194/egusphere-2026-4769
Preprint. Discussion started: 14 September 2026

3.4 WRF-CMAQ model performance

The performance of the WRF-CMAQ model was evaluated by comparing the simulated and observed time series of OH reactivity. The time series of the modeled OH reactivity was comparable to that of the calculated OH reactivity, as shown in Fig. S12. Only species with non-negligible concentrations and appreciable rate coefficients for OH radicals were included in the modeled OH reactivity (VOC species in Table S3). Because the SAPRC07 chemical mechanism represents many VOCs as lumped species, additional uncertainty was introduced in estimating the modeled OH reactivity. As shown in Fig. 5, the model substantially underestimated the OH reactivity during the daytime, particularly around noon. The largest discrepancies were associated with BVOCs and HCHO, which were both significantly underestimated relative to observations. A similar evaluation of the 2017 campaign is presented in Fig. S9, where the model exhibits the same systematic behavior but with even larger underestimations. The larger model bias in 2017 suggests that improvements in emission inventories alone are insufficient to explain the observed changes in OH reactivity between the two campaigns.

The CO concentrations were underestimated by a factor of two throughout the campaign (Fig. S13). This bias has been widely reported in previous studies on the WRF-CMAQ. For instance, Tsai et al. (2025) attributed the underestimation in Taiwan to uncertainties in emission inventories, particularly from sources with high CO/NOx emission ratios. Similarly, Tan et al. (2017) reported that the model underestimated CO concentrations during severe pollution episodes in Shanghai, where meteorological conditions, including wind fields, also contributed to model bias. They further examined a constrained scheme to improve the meteorology prediction; however, the model bias for CO was not reduced. In our constrained simulation (M2022E2017), which replaced the anthropogenic emission inventory with the 2017 inventory, the simulated CO concentration increased by 26.9%, and most of the underestimation persisted. These results suggest that uncertainties in both emission inventories and meteorological processes contribute to a persistently low bias in simulated CO concentrations, including those from cooking emissions, which are not adequately represented in the emission inventory.

In contrast to CO, the model overestimated O_3 and NO_2 by averages of 26.9% and 7.0%, respectively, under the 2022 emissions scenario. Despite these positive biases, the model reproduced the observed day-to-day variability reasonably well. The simultaneous overestimation of the sum of O_3 and NO_2 suggests that ozone production during most of the campaign occured under NOx-limited conditions, in which additional NO_2 enhanced O_3 formation. The model also reproduced the temporal variability of NO, although the peak concentrations were overestimated during episodes influenced by air masses transported from the Tokyo metropolitan area. During these episodes (e.g., the mornings of 23 and 31 August and 1 and 2 September), the positive biases in O_3 and NO_2 became less pronounced, implying a transition toward VOC-limited ozone production. A more detailed discussion of the ozone production regime is provided in Sect. 3.7. Compared with the 2022 simulation, the constrained scenario using 2017 anthropogenic emissions (M2022E2017) increased the simulated concentrations of O_3, NO_2, and NO by 7.5%, 28.3%, and 10.7%, respectively (Table S2 and Fig. S14).

https://doi.org/10.5194/egusphere-2026-4769
Preprint. Discussion started: 14 September 2026

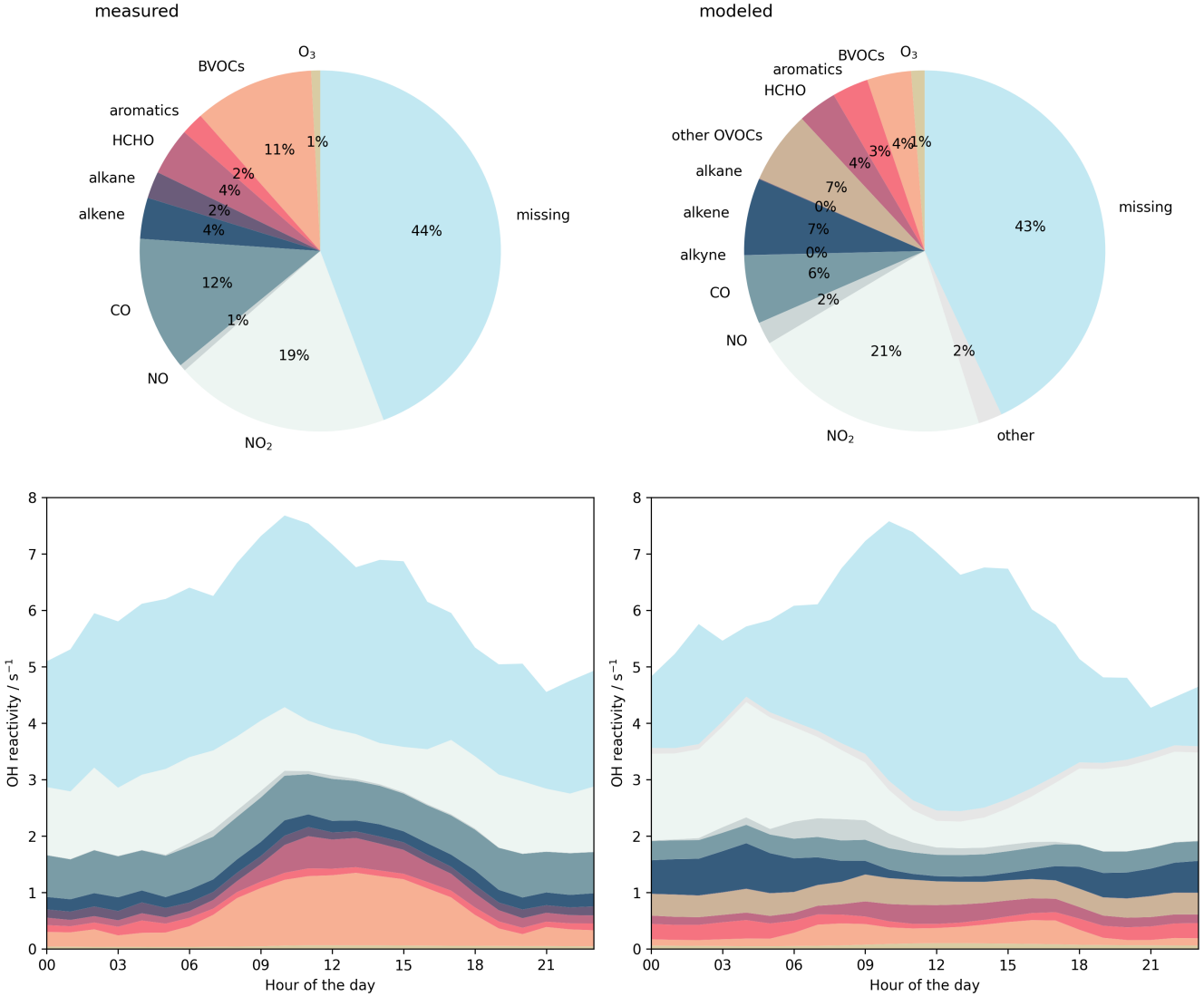

335

Figure 5. The breakdown (upper panel) and hourly diel averages (bottom panel) of total OH reactivity by measured (left side) and modeled trace species from WRF-CMAQ simulation (right side).

3.5 HCHO formation and missing secondary products

340 Unlike CO, which exhibited relatively weak diurnal variability (Fig. 6), HCHO exhibited a pronounced daytime increase, indicating substantial secondary photochemical production. As shown in both the diurnal cycle (Fig. 6) and the time series (Fig. S15), the WRF-CMAQ model substantially underestimated HCHO during the daytime and slightly overestimated it at

https://doi.org/10.5194/egusphere-2026-4769
Preprint. Discussion started: 14 September 2026

night. During the campaign, hourly HCHO concentrations ranged from 0.03 to 6.5 ppbv in the observations, 0.36 to 3.4 ppbv in the 2022 simulation, and 0.56 to 4.9 ppbv in the constrained simulation (M2022E2017). The largest daytime underestimation occurred on 26 and 27 August, coinciding with the periods when the model substantially overestimated O_3. Replacing the anthropogenic emissions inventory with the 2017 inventory increased the simulated HCHO concentration by approximately 20% on average. This enhancement was slightly more pronounced at night than during the day, indicating that primary HCHO emissions dominated nighttime concentrations, whereas daytime HCHO emissions were strongly influenced by photochemical production.

The ratio of HCHO to CO was analyzed to distinguish primary emissions from secondary formation (Fig. S16). During the daytime, photochemical oxidation enhances secondary HCHO production, increasing the HCHO/CO ratio. Therefore, the minimal nocturnal HCHO/CO ratio was used to represent the primary emission ratio, allowing the estimation of secondary HCHO fraction (lower panel in Fig. 6). This approach was evaluated against independent methods, including linear regression analysis and photochemical decay retrieval, and yielded consistent results (Fukusaki et al., 2026). Based on these observations, the contribution of primary HCHO began to decrease after 05:00 LT, reached a minimum of approximately 20% at noon, and subsequently increased after 15:00 LT, exceeding 90% after midnight. The simulations reproduced the overall diurnal pattern but consistently overestimated the contribution from primary HCHO, indicating an underestimation of secondary HCHO formation. The maximum secondary HCHO fraction reached 52% and 45% in the 2022 and constrained simulations, respectively, which were 28% and 35% lower than the observation-based estimates. These results are consistent with the underestimation of HCHO's contribution to OH reactivity, specifically during the daytime when the model underestimated the HCHO concentration by approximately 33% (Table 3). Together, these findings suggest that the model fails to adequately represent secondary HCHO production, contributing to the underestimation of total OH reactivity.

https://doi.org/10.5194/egusphere-2026-4769
Preprint. Discussion started: 14 September 2026

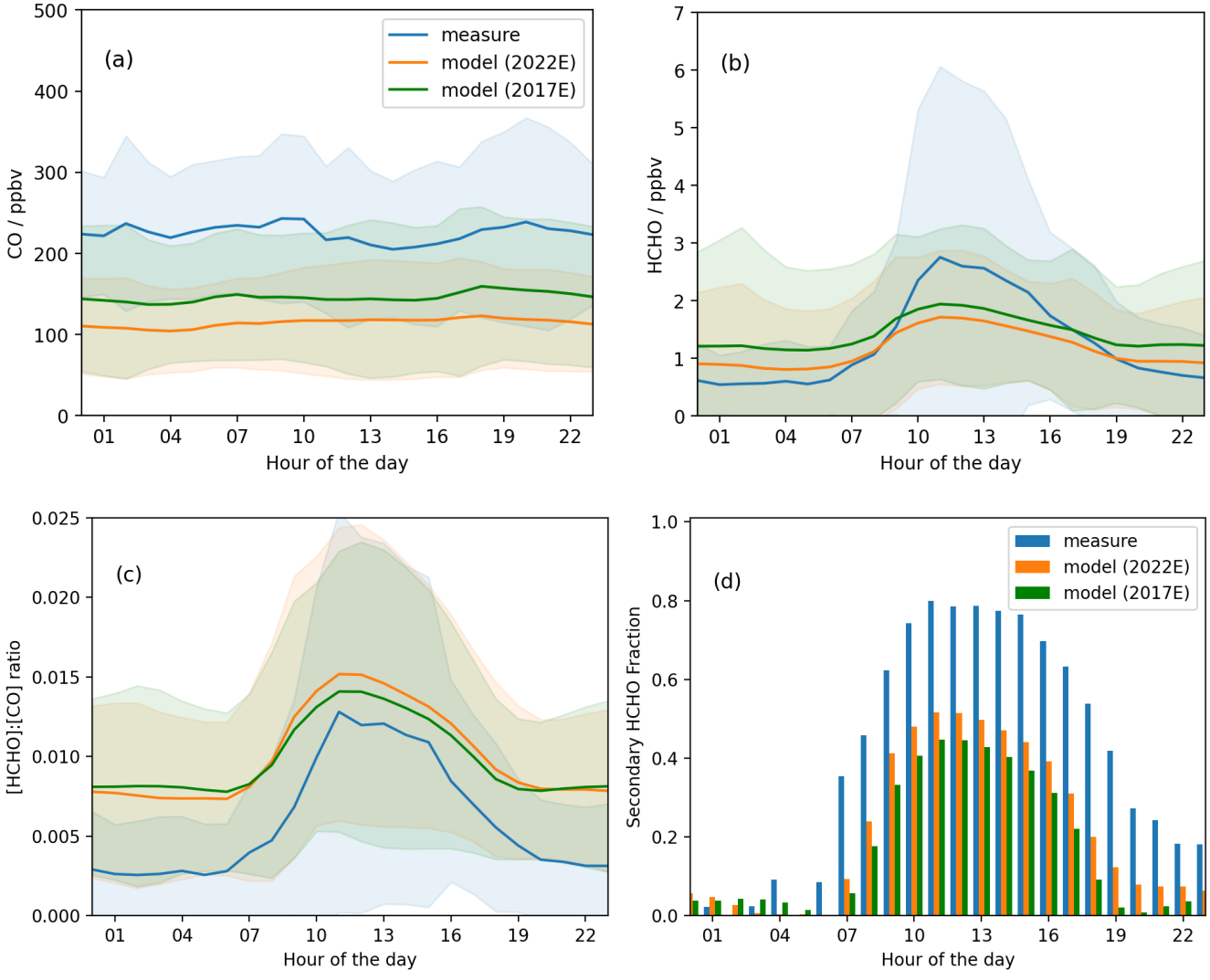

Figure 6. The diel variations of CO (a), HCHO (b), HCHO-to-CO ratio (c), and fraction of secondary HCHO (d) based on the emission ratio method using the HCHO-to-CO ratio. Measured results are in blue, modeled results are in orange, and those from the constrained model with 2017 emissions are in green. The colored stock area indicates the uncertainty range at 2 σ.

The relationship between HCHO and missing OH reactivity was further examined because previous smog-chamber experiments demonstrated a strong linear correlation between HCHO concentration and missing OH reactivity, indicating the co-production of HCHO and highly reactive dicarbonyl compounds during VOC oxidation (Li et al., 2025). This relationship was also observed during the 2017 Tsukuba field campaign (Li et al., 2025). However, applying the same empirical relationship to the 2022 observations resulted in substantial discrepancies, particularly during nighttime (Fig. 7). As shown in Fig. S17, HCHO remained moderately correlated with the missing OH reactivity during the daytime, whereas no significant correlation was observed at night. This result suggests that the missing OH reactivity during nighttime cannot be explained solely by the

https://doi.org/10.5194/egusphere-2026-4769
Preprint. Discussion started: 14 September 2026

secondary oxidation products associated with HCHO formation. Instead, the elevated nighttime missing OH reactivity is likely attributable to primary reactive species transported from the south that were not measured during the field campaign and were also absent from the current model simulation.

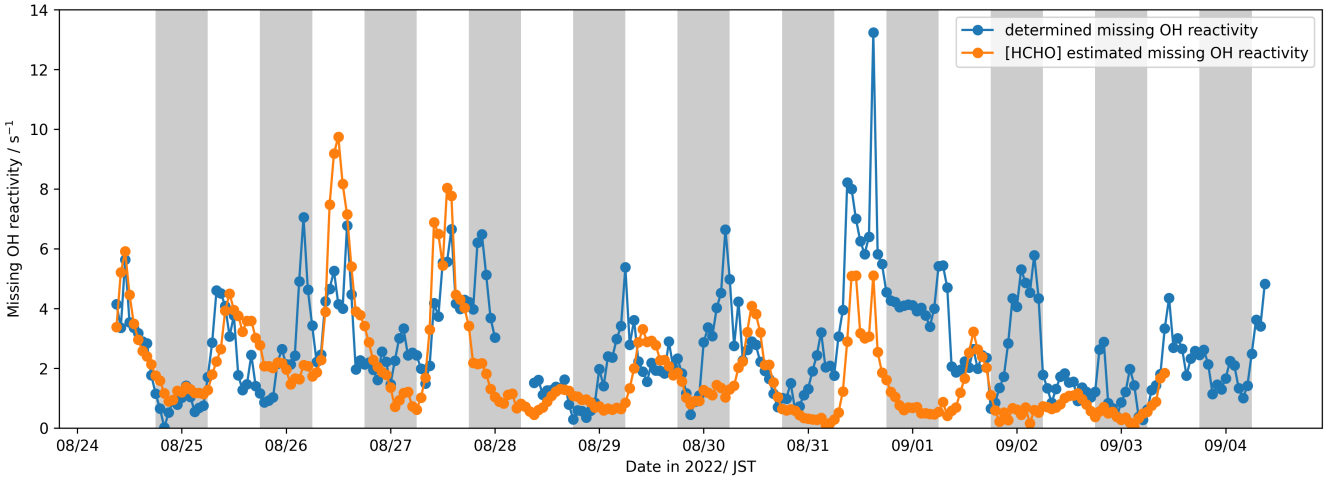

Figure 7. Diurnal variations of the missing OH reactivity from observations and from the measured HCHO concentration using $k'_{missing}/[HCHO]=1.5\ s^{-1}\ ppbv^{-1}$.

3.6 XO_2 budget analysis

The XO_2 ($\equiv HO_2 + RO_2$) budget provides valuable insight into the atmospheric oxidation capacity and serves as an independent evaluation of the model's performance. The PERCA-CAPS instrument measures the total XO_2 concentration; therefore, the modeled XO_2 concentration was calculated as the sum of the simulated HO_2 and all RO_2 species for each simulation scenario. As shown in Fig. 8, the observed XO_2 concentrations exhibited multiple spikes on rainy days, such as 28 and 30 August and 1 September. These fluctuations may be associated with rapidly changing meteorological conditions and rain-induced soil NOx emissions (Ghude et al., 2010), which tend to introduce bias into the measurements. On most of the other days, the model reproduced the observed day-to-day variability reasonably well, with only a modest bias. Part of the remaining discrepancy may be related to the measurement interference from the thermal decomposition of HO_2NO_2 and RO_2NO_2, which was quantified and corrected in the PERCA system (Sakamoto et al., 2026).

The constraint simulation (M2022E2017) slightly reduced the daily peak XO_2 concentrations because the increased emissions enhanced radical termination reactions. The three largest model underestimations occurred on the 23 and 31 August, and on 1 September, coinciding with periods when NO concentrations were substantially overestimated. The elevated NO promoted the conversion of peroxyl radicals to OH, thereby reducing the simulated XO_2 concentrations. Consistent with this interpretation,

https://doi.org/10.5194/egusphere-2026-4769
Preprint. Discussion started: 14 September 2026

Fig. S18 shows that PAN decomposition's contribution to P_{HOx} was suppressed during these episodes. In contrast, the model overestimated XO_2 on 26 and 30 August, which may be attributable to an underestimation of NO_2, leading to weaker radical termination and consequently higher simulated XO_2 concentrations.

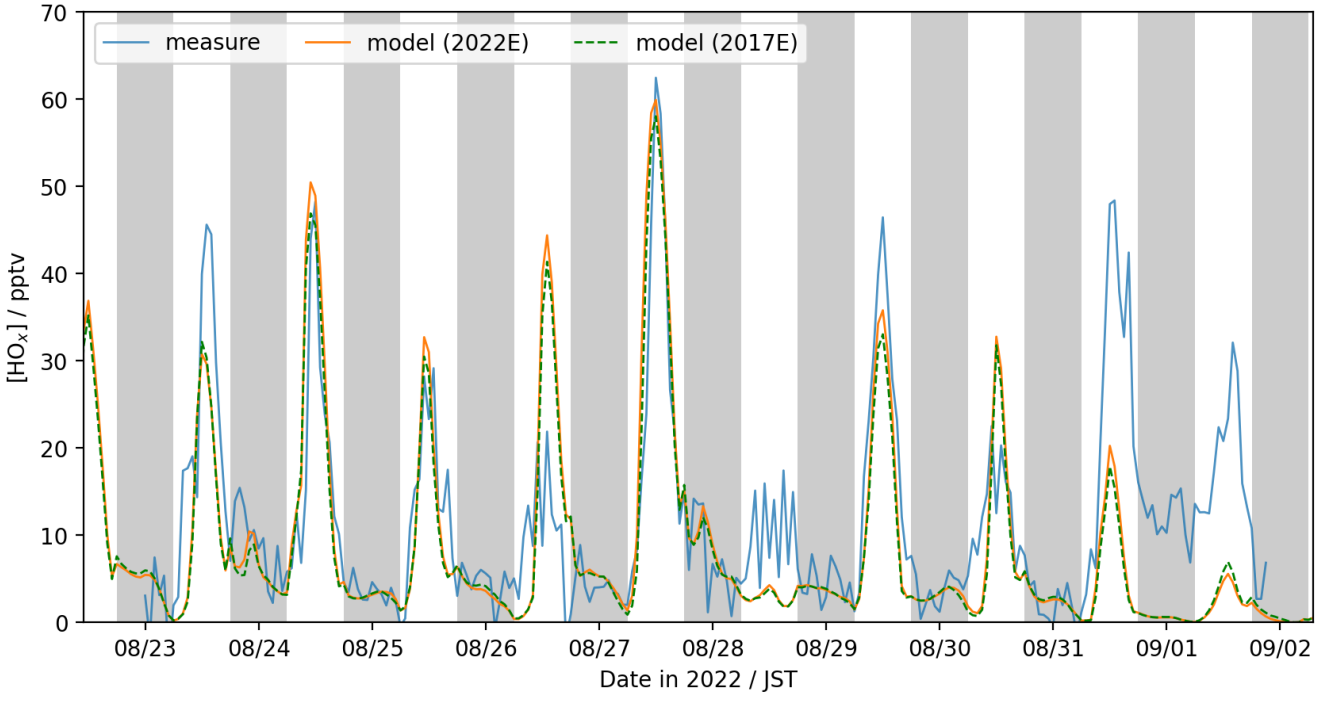

Figure 8. Time series of XO_2 concentrations from measurements (in blue), simulation (in orange), and constrained simulation using 2017 emission inventories (in green).

3.7 Ozone production sensitivity

Ozone production sensitivity was evaluated to identify whether ozone formation was primarily limited by VOCs or NOx. Based on field observations, the ozone production regime was first classified using the k_{VOC}/k_{NOx} and $HCHO/NO_2$ ratios, following the index values proposed in smog-chamber experiments (Li et al., 2025). The k_{VOC}/k_{NOx} ratio has been validated against direct observations of ozone production rates during an industrial field campaign (Sadanaga et al., 2026). In addition, the HOx budget indicator, L_N/Q, was applied, where L_N represents radical termination by NOx and Q denotes the total radical production that sustains the photochemical chain reactions (Kleinman, 2005; Kleinman et al., 1997, 2001). The transition regime defined by L_N/Q_{trans} corresponds to the equal sensitivity of ozone production to VOC and NOx. The HOx budget indicator was further developed for heterogeneous HO_2 uptake following Sakamoto et al. (2019). A constant first-order HO_2 heterogeneous loss rate of 0.0023 s^{-1} based on the measurements at a suburban site (Li et al., 2022) can be used. Finally, we

https://doi.org/10.5194/egusphere-2026-4769
Preprint. Discussion started: 14 September 2026

propose a new classification method that combines the k_{VOC}/k_{NOx} ratio with NO concentration. The performance and limitations of these approaches were compared using observations from the 2022 Tsukuba campaign.

3.7.1 k_{VOC}/k_{NOx} and $HCHO/NO_2$ ratios

Figure 9 (a) and (b) compare the ozone regime using two traditional index approaches: the k_{VOC}/k_{NOx} ratio, and $HCHO/NO_2$ ratios, respectively. The NOx-limited regime was observed for k_{VOC}/k_{NOx} ratios greater than 7.4–9.1, depending on the initial mixing ratios of the air (Li et al., 2025; Sadanaga et al., 2026). Thus, we highlighted the period with a ratio larger than 7.4 in light red and labeled it "transition to NOx-limited," and the period with a ratio larger than 9.1 in dense red as "NOx-limited." The reactivity ratio from the top-down measurement exceeded 7.4 at noon on 24, 27, and 31 August, and on 3 and 4 September, as highlighted in Fig. 9 (a). The ratio from both bottom-up measurement and simulations was, in most cases, smaller than 7.4; therefore, we may expect a dominant role for the VOC-limited regime. Figure S19 compares the time series of the VOC and NOx reactivities from the measurements and model simulations. Bottom-up measurements and simulations largely underestimated VOC reactivity due to the missing OH reactivity, causing estimation uncertainties. NOx reactivity was generally well reproduced until 2 September, and sharp nocturnal overestimates appeared on 2 and 3 September.

Similarly, the results based on the $HCHO/NO_2$ ratio showed NOx-limited regimes on 24, 25, and 27 August, and briefly on 31 August, in both the measured and modeled ratios. However, the modeled ratio was also larger than the index of 1.4 on 26 and 29 August. This discrepancy was primarily caused by the model's underestimation of NO_2 (see Fig. S14), which had larger concentrations and wider temporal variability than HCHO (Fig. S15). Although the smog-chamber study recommends a transition-range index of 1.4–2.1 (Li et al., 2025), we observed an $HCHO/NO_2$ ratio below 2.1 throughout the campaign and thus defined the NOx-limited regime as ratios above 1.4. The days 28 and 30 August and 1–3 September were classified as "VOC-limited" regimes from both measured and modeled $HCHO/NO_2$ ratios.

https://doi.org/10.5194/egusphere-2026-4769
Preprint. Discussion started: 14 September 2026

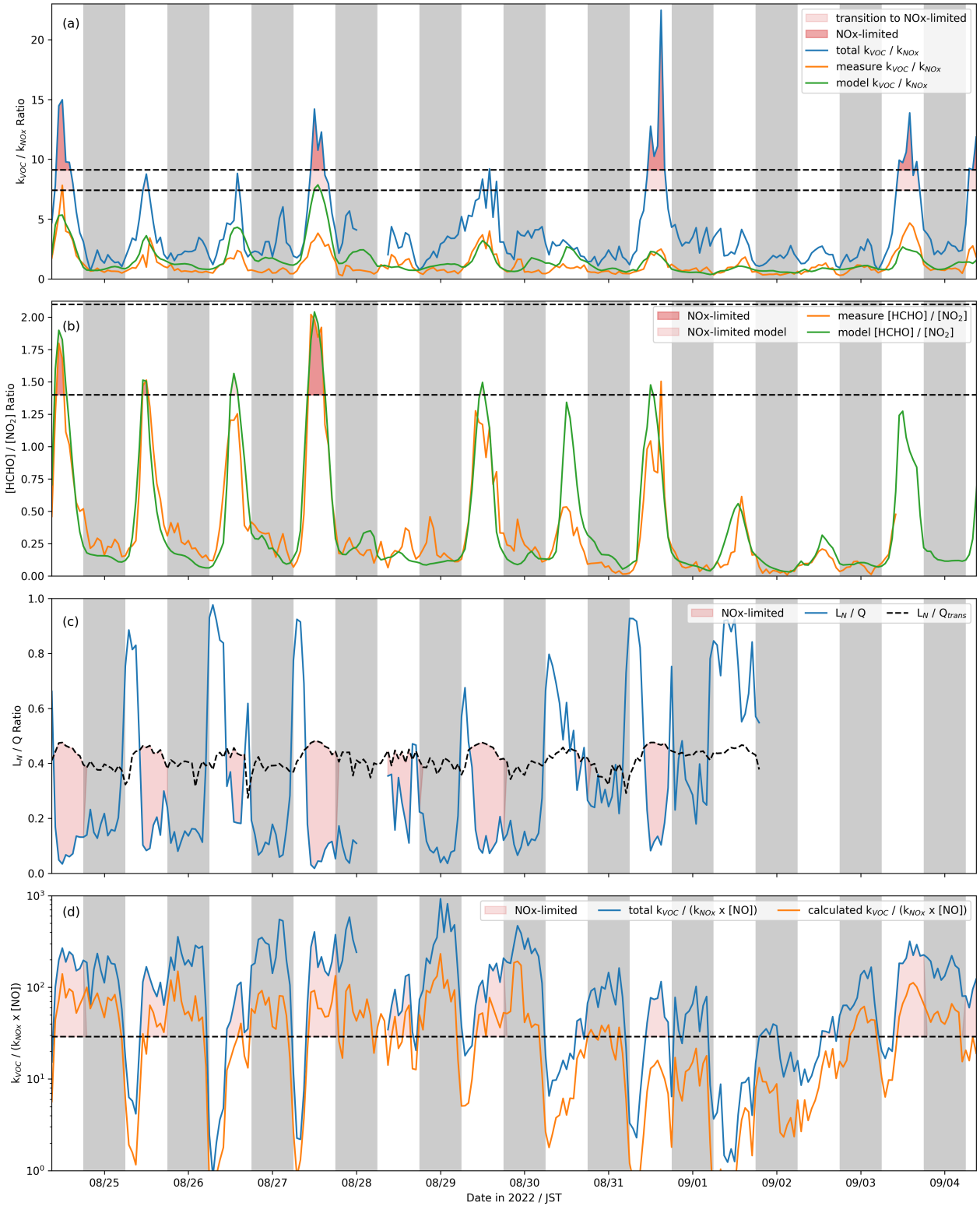

https://doi.org/10.5194/egusphere-2026-4769
Preprint. Discussion started: 14 September 2026

Figure 9. Top to bottom: ozone regime classification results from the index of k_{VOC}/k_{NOx}, [HCHO]/[NO_2], L_N/Q, and the empirical method proposed from k_{VOC}/k_{NOx} and [NO] relationship. The NOx-limited regime condition is highlighted in red. Dashed lines in each panel indicate the corresponding transition regime.

3.7.2 Radical budget balance

L_N/Q acts as an efficient proxy for determining ozone regime sensitivity. Equation (2) is adopted from Sakamoto et al. (2019). When there is no heterogeneous XO_2 loss, L_N/Q_{trans} = ½ is used to separate the VOC- and NOx-limited conditions (Kleinman et al., 1997). Considering heterogeneous HOx loss, the transition equation, Eq. (3), is modulated by the ratio of heterogeneous XO_2 loss (L_P) to the sum of L_P and XO_2 self-cross reaction losses (L_R), as shown in Eq. (4).

$$\frac{L_N}{Q} = \frac{1}{1+\left(\frac{2k_{eff}[XO_2]+k'_{PU\_HOx}}{k_{HO2-NO}\beta}\right)\cdot\frac{k_i[VOC]_i}{k_{NO2}[NO_2]}\cdot\frac{1}{[NO]}} \quad (2)$$

$$\frac{L_N}{Q_{trans}} = \frac{3-\chi}{6} \quad (3)$$

$$\chi = \frac{L_P}{L_P+L_R} = \frac{k'_{PU\_HOx}}{k'_{PU\_HO2}+2k_{eff}[HO_x]} \quad (4)$$

$$k_{eff} = k_{HO2-HO2}\cdot(\beta)^2 + k_{HO2-RO2}\cdot\beta\cdot(1-\beta) \quad (5)$$

The parameters in Eqs. (2)–(4) are XO_2 concentration ([XO_2]), NO_2 concentration ([NO_2]), NO concentration ([NO]), the ratio of HO_2 over XO_2 radicals (β), the rate constants of OH with NO_2 (k_N) and HO_2 with NO ($k_{HO2\text{-}NO}$). k'_{PU_HO2} considers only the heterogeneous HO_2 loss, which is used as 0.0023 s^{-1} (Li et al., 2022). k_{eff} is the effective bimolecular HO_2/RO_2 radical rate constant balanced by β, as denoted by Eq. (5). The effective HO_2 self-reaction rate constant, $k_{HO2\text{-}HO2}$, was derived by considering the equilibrium formation of the HO_2-H_2O complex, as proposed by Kanno et al. (2006). $k_{HO2\text{-}RO2}$ uses a temperature-dependent rate constant derived from the rate constant at 298 K (Orlando and Tyndall, 2012). $k_i[VOC]_i$ refers to the OH reactivity derived from the reaction with VOCs, including missing OH reactivity, and reaction with CO and O_3.

Figure 9 (c) shows the "NOx-limited" regime in the red-highlighted region. Due to the data availability, we reported results only from 24 August to 1 September. Almost every day (except 1 September) was NOx-limited during most of the daytime, with a short VOC-limited period in the morning. Compared with the results of the 2017 Tsukuba campaign (Sakamoto et al., 2019), the NOx-limited regime increased during the 2022 campaign. The results based on L_N/Q without aerosol uptake are shown in Fig. S20. The NOx-limited regime expanded upon consideration of aerosol uptake, consistent with the conclusions of previous field campaigns (Kohno et al., 2022; Li et al., 2022) and a chamber experiment (Sato et al., 2026). When comparing the results in Figs. 9 (c) and S20, the regime transitioned from VOC-limited to NOx-limited, occurring briefly at noon or in the afternoon on 25, 26, and 28 August due to the aerosol uptake effect.

3.7.3 An NO-corrected k_{VOC}/k_{NOx} index

https://doi.org/10.5194/egusphere-2026-4769
Preprint. Discussion started: 14 September 2026

Owing to the inconsistency of the NOx-limited period in Fig. 9 (a), (b), and (c), we propose a new method to distinguish VOC- and NOx-limited regimes, which is derived from the theory of L_N/Q. Equations (2) and Eq (3) can be transformed into Eq. (6) to extrapolate the relationship between k_{VOC}/k_{NOx} and [NO] as follows:

$$\frac{k_{VOC}}{k_{NOx}} = \frac{k_i[VOC]_i}{k_{NO2}[NO_2]+k_{NO}[NO]} \leq \frac{k_i[VOC]_i}{k_{NO2}[NO_2]} = \frac{3+\chi}{3-\chi} \cdot \frac{k_{HO2-NO}\beta}{(2k_{eff}[XO_2]+k'_{PU_{HO2}})} \cdot [NO] \quad (6)$$

The equation can then be simplified as:

$$\frac{k_{VOC}}{k_{NOx_{trans}}} = \delta \cdot [NO] \quad (7)$$

Where, $\delta = \frac{3+\chi}{3-\chi} \cdot \frac{k_{HO2-NO}\beta}{(2k_{eff}[XO_2]+k'_{PU_{HO2}})}$, and an approximation value of δ was identified as 28.9 $ppbv^{-1}$ from Fig. 7 of our previous work (Li et al., 2022). A sensitivity test of δ as a function of k'_{PU_HO2} and $k_{eff} \cdot [XO_2]$ is provided in Fig. S21. Although δ varies with the input parameters, in most cases it falls in the range of 10–50 (Fig. S21). In case of using an assumed k'_{PU_HO2} as 0.0023 s^{-1}, an average δ value of 28.9 recommended from previous literature also fits well in the 2022 Tsukuba campaign. Generally, the increase of k'_{PU_HO2} will reduce δ, which consequently leads to a more NOx-limited regime given the same level of radical self/cross reactions. On the other hand, the enhanced XO_2 self/cross reactions ($k_{eff} \cdot [XO_2]$) will also reduce δ and shift to the NOx-limited regime. We could assign the condition standard as explained hereafter:

If $\frac{k_{VOC}}{k_{NOx}} \geq 28.9 \times [NO]$, which is a NOx-limited regime.

Or $\frac{k_{VOC}}{k_{NOx}} \leq 28.9 \times [NO]$, which is a VOC-limited regime.

This new index uses k_{VOC}/k_{NOx} and NO concentration to assess ozone production sensitivity and does not require $[XO_2]$, the HO_2/XO_2 ratio, the XO_2 self/cross-reaction rate, or the heterogeneous HO_2 loss rate, and so on. This simplified method is easier to apply than the radical budget balance method and more precise than the simple $HCHO/NO_2$ and reactivity ratio methods. NO concentration is required here is because the ozone regime transition is sensitive to NO depletion. The NO reactivity is added to the left side of Eq. (6), which reduces the reactive ratio by approximately 5%. Under NO concentrations above 0.3 ppbv, the reactivity ratio (k_{VOC}/k_{NOx}) is sufficient to assess the ozone production regime. We previously conducted a campaign in the industry area, where the average NO concentration was 7.8 ppbv, with daily average ranging from 2.8 to 13.3 ppbv (Li et al., 2021). The direct evaluation of the ozone production regime in the same campaign agreed well with the results obtained using the k_{VOC}/k_{NOx} index (Sadanaga et al., 2026). However, in the case of low NO, as in the current study, the uncertainties increased with decreasing NO concentration. This also explains the limitations of traditional index results, as shown in Fig. 9 (a). Note that this method's larger uncertainty is also expected at low NO concentrations, owing to detection limit bias.

https://doi.org/10.5194/egusphere-2026-4769
Preprint. Discussion started: 14 September 2026

The results obtained with this new index in the 2022 Tsukuba campaign are shown in Fig. 9 (d) and are in good agreement with the radical budget balance method using L_N/Q. The new index was tested during the 2017 Tsukuba campaign (Fig. S22). Except for the first day, all remaining days were consistent with the results obtained using L_N/Q from Fig. 1 in Sakamoto et al. (2019). Compared with the traditional index, we suggest using this index to clarify the ozone production regime and avoid overestimating the VOC-limited regime under low NO conditions. The k_{VOC}/k_{NOx} ratio, based on the calculated OH reactivity, is plotted as an orange line in Fig. 9 (d), which periodically underestimates the NOx-limited regime and underscores the significance of the missing OH reactivity. Grouping all unidentified trace species into VOC may shift the VOC-limited regime to a NOx-limited regime. This emphasizes the importance of unidentified reactive gases and NOx mitigation, which may be overlooked in general cases.

4 Conclusions

The 2022 AQUAS–Tsukuba campaign observed a substantial reduction in NOx and VOCs and retained approximately half of the total OH reactivity compared with the 2017 Tsukuba campaign. Given that the meteorological conditions were more active in 2022, the primary emission reduction was partially offset by stronger transported air masses. However, secondary products such as ozone remained at a level comparable to that in 2017 (overall ozone average was 28.3 ± 11.2 ppbv in 2022 versus 31.1 ± 20.4 ppbv in 2017), which was enhanced by the transition of ozone regime driven by the different change rates of ozone precursors. HCHO, a representative of oxygenated trace species that originates from both direct emissions and secondary production, was found to be dominantly contributed by secondary emissions in the daytime. Owing to both the meteorological conditions and the active chemical transformation processes, the atmospheric oxidation capacity remained active to sustain ozone formation. WRF-CMAQ underestimated the total OH reactivity, with 43% unexplained, primarily due to underestimation of BVOCs and OVOCs at noon. The largest underprediction occurred for the southern wind passing through the Tokyo area. The model's performance degraded at high wind speeds, suggesting that transported air pollutants and their oxidant products were partly missed by the model and were subject to meteorological bias. We obtained good overall agreement between the measured and modeled XO_2 concentrations, except for discrepancies due to precipitation and disagreement over NOx. Ozone regime typically began as a "VOC-limited" regime in the morning and soon transitioned to a "NOx-limited" regime during the 2022 Tsukuba campaign. The traditional ozone regime indicator may overestimate the "VOC-limited" regime due to the index's conditional bias. Therefore, a case-by-case correction is required. We recommend using the condition of— $\frac{k_{VOC}}{k_{NOx}} = \mathbf{28.9 \times [NO]}$; NO in ppbv—for the ozone regime, which showed consistent results with the radical budget balance method using the L_N/Q index. Further application of this new index is required to assess broader

https://doi.org/10.5194/egusphere-2026-4769
Preprint. Discussion started: 14 September 2026

atmospheric implications, particularly under conditions with varied NOx competing gas-phase reactions, and heterogeneous HOx termination reactions.

Data availability

The data will be publicly accessible after the publication of the 2022 AQUAS–Tsukuba campaign series. The readers are recommended to refer to the newest article of the 2022 AQUAS–Tsukuba Campaign: Part II.

Supplement link

The link to the supplement will be included by Copernicus, if applicable.

Author contributions

Jiaru Li: Investigation, Data curation, Validation, Visualization, Writing original draft, Writing review and editing, Funding acquisition, Conceptualization; Yosuke Sakamoto: Investigation, Data curation, Supervision, Project administration, Conceptualization; Egami Kouichi: Investigation, Data curation; Yu Morino: Formal analysis, Software, Data curation; Kei Sato: Investigation, Data curation; Nanase Kohno: Investigation, Data curation; Yasuhiro Sadanaga: Investigation, Data curation; Shungo Kato: Investigation, Data curation; Yoshihiro Nakashima: Investigation, Data curation; Ayako Yoshino: Investigation, Data curation; Akinori Takami: Investigation, Data curation; Yugo Kanaya: Writing review and editing, Supervision; Yoshizumi Kajii: Funding acquisition, Conceptualization, Supervision.

Competing interests

At least one of the (co-)authors is a member of the editorial board of Atmospheric Chemistry and Physics.

Disclaimer

Copernicus Publications remains neutral regarding jurisdictional claims made in the text, published maps, institutional affiliations, or any other geographical representation in this paper. While Copernicus Publications makes every effort to include appropriate place names, the final responsibility lies with the authors. Views expressed in the text are those of the authors and do not necessarily reflect the views of the publisher.

https://doi.org/10.5194/egusphere-2026-4769
Preprint. Discussion started: 14 September 2026

Acknowledgements

The authors are grateful to the Air Quality Research Station of the National Institute for Environmental Studies for their assistance with the observations. The authors acknowledge Dr. Kentaro Murano, Lyu Xinyao, and Humm Kham Zan Zan Aung for their assistance during the campaign. The authors also thank Editage for the English editing. The authors used Cursor for data analysis and reviewed and edited the code as needed and take full responsibility for the content of the published article.

Financial support

This work was supported by the Japan Society for the Promotion of Science (JSPS) KAKENHI (JP16H06305, JP19H04255, JP21H04926, JP23K17029, JP26K21432), the Environment Research and Technology Development Fund (JPMEERF20215002) of the Environmental Restoration and Conservation Agency, Japan, and the FY2021 National Institute for Environmental Studies Research Funding (2526AN001).

Review statement

The review statement will be added by Copernicus Publications listing the handling editor as well as all contributing referees according to their status anonymous or identified.

References

Brune, W. H., Miller, D. O., Thames, A. B., Brosius, A. L., Barletta, B., Blake, D. R., Blake, N. J., Chen, G., Choi, Y., Crawford, J. H., Digangi, J. P., Diskin, G., Fried, A., Hall, S. R., Hanisco, T. F., Huey, G. L., Hughes, S. C., Kim, M., Meinardi, S., Montzka, D. D., Pusede, S. E., Schroeder, J. R., Teng, A., Tanner, D. J., Ullmann, K., Walega, J., Weinheimer, A., Wisthaler, A., and Wennberg, P. O.: Observations of atmospheric oxidation and ozone production in South Korea, Atmospheric Environment, 269, 118854, https://doi.org/10.1016/j.atmosenv.2021.118854, 2022.

Calvin, K., Dasgupta, D., Krinner, G., Mukherji, A., Thorne, P. W., Trisos, C., Romero, J., Aldunce, P., Barrett, K., Blanco, G., Cheung, W. W. L., Connors, S., Denton, F., Diongue-Niang, A., Dodman, D., Garschagen, M., Geden, O., Hayward, B., Jones, C., Jotzo, F., Krug, T., Lasco, R., Lee, Y.-Y., Masson-Delmotte, V., Meinshausen, M., Mintenbeck, K., Mokssit, A., Otto, F. E. L., Pathak, M., Pirani, A., Poloczanska, E., Pörtner, H.-O., Revi, A., Roberts, D. C., Roy, J., Ruane, A. C., Skea, J., Shukla, P. R., Slade, R., Slangen, A., Sokona, Y., Sörensson, A. A., Tignor, M., Van Vuuren, D., Wei, Y.-M., Winkler, H., Zhai, P., Zommers, Z., Hourcade, J.-C., Johnson, F. X., Pachauri, S., Simpson, N. P., Singh, C., Thomas, A., Totin, E., Alegría, A., Armour, K., Bednar-Friedl, B., Blok, K., Cissé, G., Dentener, F., Eriksen, S., Fischer, E., Garner, G., Guivarch, C., Haasnoot, M., Hansen, G., Hauser, M., Hawkins, E., Hermans, T., Kopp, R., Leprince-Ringuet, N., Lewis, J., Ley, D., Ludden, C., Niamir, L., Nicholls, Z., Some, S., Szopa, S., Trewin, B., Van Der Wijst, K.-I., Winter, G., Witting, M., Birt, A., and Ha, M.: IPCC, 2023: Climate Change 2023: Synthesis Report. Contribution of Working Groups I, II and III to the Sixth Assessment Report of the Intergovernmental Panel on Climate Change [Core Writing Team, H. Lee and J. Romero (eds.)]. IPCC, Geneva, Switzerland., Intergovernmental Panel on Climate Change (IPCC), https://doi.org/10.59327/IPCC/AR6-9789291691647, 2023.

https://doi.org/10.5194/egusphere-2026-4769
Preprint. Discussion started: 14 September 2026

Cantrell, C. A. and Stedman, D. H.: A possible technique for the measurement of atmospheric peroxy radicals, Geophysical Research Letters, 9, 846–849, 1982.

Carn, S. A., Fioletov, V. E., McLinden, C. A., Li, C., and Krotkov, N. A.: A decade of global volcanic SO2 emissions measured from space, Sci Rep, 7, 44095, https://doi.org/10.1038/srep44095, 2017.

Chatani, S., Shimo, N., Matsunaga, S., Kajii, Y., Kato, S., Nakashima, Y., Miyazaki, K., Ishii, K., and Ueno, H.: Sensitivity analyses of OH missing sinks over Tokyo metropolitan area in the summer of 2007, Atmos. Chem. Phys., 2009.

Fukusaki Y., Sadanaga Y., Nakashima Y., Sato K., Ramasamy S., Nakayama T., Kohno N., Sakamoto Y., and Kajii Y.: 横浜市臨海部における大気中ホルムアルデヒドの一次排出および二次生成寄与の算出, https://doi.org/10.11298/taiki.61.35, 7 April 2026.

Ghude, S. D., Lal, D. M., Beig, G., Van Der A, R., and Sable, D.: Rain-Induced Soil NO_x Emission From India During the Onset of the Summer Monsoon: A Satellite Perspective, J. Geophys. Res., 115, 2009JD013367, https://doi.org/10.1029/2009JD013367, 2010.

Hansen, R. F., Griffith, S. M., Dusanter, S., Rickly, P. S., Stevens, P. S., Bertman, S. B., Carroll, M. A., Erickson, M. H., Flynn, J. H., Grossberg, N., Jobson, B. T., Lefer, B. L., and Wallace, H. W.: Measurements of total hydroxyl radical reactivity during CABINEX 2009 – Part 1: field measurements, Atmos. Chem. Phys., 2014.

Hansen, R. F., Blocquet, M., Schoemaecker, C., Léonardis, T., Locoge, N., Fittschen, C., Hanoune, B., Stevens, P. S., Sinha, V., and Dusanter, S.: Intercomparison of the comparative reactivity method (CRM) and pump-probe technique for measuring total OH reactivity in an urban environment, Atmospheric Measurement Techniques, 8, 4243–4264, https://doi.org/10.5194/amt-8-4243-2015, 2015.

Kanno, N., Tonokura, K., and Koshi, M.: Equilibrium constant of the HO_2-H_2O complex formation and kinetics of HO_2 +HO_2-H_2O: Implications for tropospheric chemistry, Journal of Geophysical Research Atmospheres, 111, 1–7, https://doi.org/10.1029/2005JD006805, 2006.

Kleinman, L. I.: The dependence of tropospheric ozone production rate on ozone precursors, Atmospheric Environment, 39, 575–586, https://doi.org/10.1016/j.atmosenv.2004.08.047, 2005.

Kleinman, L. I., Daum, P. H., Lee, J. H., Lee, Y. N., Nunnermacker, L. J., Springston, S. R., Newman, L., Weiristein-Lloyd, J., and Sillman, S.: Dependence of ozone production on NO and hydrocarbons in the troposphere, Geophysical Research Letters, 24, 2299–2302, https://doi.org/10.1029/97GL02279, 1997.

Kleinman, L. I., Daum, P. H., Lee, Y. N., Nunnermacker, L. J., Springston, S. R., Weinstein-Lloyd, J., and Rudolph, J.: Sensitivity of ozone production rate to ozone precursors, Geophysical Research Letters, 28, 2903–2906, https://doi.org/10.1029/2000GL012597, 2001.

Kohno, N., Zhou, J., Li, J., Takemura, M., Ono, N., Sadanaga, Y., Nakashima, Y., Sato, K., Kato, S., Sakamoto, Y., and Kajii, Y.: Impacts of missing OH reactivity and aerosol uptake of HO2 radicals on tropospheric O3 production during the AQUAS-Kyoto summer campaign in 2018, Atmospheric Environment, 281, 119130, https://doi.org/10.1016/j.atmosenv.2022.119130, 2022.

Kovacs, T. A. and Brune, W. H.: Total OH Loss Rate Measurement, Journal of atmospheric chemistry, 39, 105–122, https://doi.org/10.1186/s12876-015-0381-4, 2001.

https://doi.org/10.5194/egusphere-2026-4769
Preprint. Discussion started: 14 September 2026

Kovacs, T. A., Brune, W. H., Harder, H., Martinez, M., Simpas, J. B., Frost, G. J., Williams, E., Jobson, T., Stroud, C., Young, V., Fried, A., and Wert, B.: Direct measurements of urban OH reactivity during Nashville SOS in summer 1999, Journal of Environmental Monitoring, 5, 68–74, https://doi.org/10.1039/b204339d, 2003.

Lee, J. D., Young, J. C., Read, K. A., Hamilton, J. F., Hopkins, J. R., Lewis, A. C., Bandy, B. J., Davey, J., Edwards, P., Ingham, T., Self, D. E., Smith, S. C., Pilling, M. J., and Heard, D. E.: Measurement and calculation of OH reactivity at a United Kingdom coastal site, J Atmos Chem, 64, 53–76, https://doi.org/10.1007/s10874-010-9171-0, 2009.

Li, J., Sakamoto, Y., Kohno, N., Fujii, T., Matsuoka, K., Takemura, M., Zhou, J., Nakagawa, M., Murano, K., Sadanaga, Y., Nakashima, Y., Sato, K., Takami, A., Yoshino, A., Nakayama, T., Kato, S., and Kajii, Y.: Total hydroxyl radical reactivity measurements in a suburban area during AQUAS–Tsukuba campaign in summer 2017, Science of the Total Environment, 740, 139897, https://doi.org/10.1016/j.scitotenv.2020.139897, 2020.

Li, J., Kohno, N., Sakamoto, Y., Fukusaki, Y., Kousa, Y., Sadanaga, Y., Nakashima, Y., Sato, K., Ramasamy, S., Takami, A., Yoshino, A., Nakayama, T., Kato, S., Ono, N., Zhou, J., Bai, Y., and Kajii, Y.: A quantitative understanding of total OH reactivity and ozone production in a coastal industrial area during the Yokohama air quality study (AQUAS) campaign of summer 2019, Atmospheric Environment, 267, https://doi.org/10.1016/j.atmosenv.2021.118754, 2021.

Li, J., Kohno, N., Sakamoto, Y., Pham, H. G., Murano, K., Sato, K., Nakayama, T., and Kajii, Y.: Potential Factors Contributing to Ozone Production in AQUAS-Kyoto Campaign in Summer 2020: Natural Source-Related Missing OH Reactivity and Heterogeneous HO2/RO2Loss, Environmental Science and Technology, 56, 12926–12936, https://doi.org/10.1021/acs.est.2c03628, 2022.

Li, J., Miyatake, K., Morino, Y., Sato, K., Sadanaga, Y., Nakashima, Y., Sakamoto, Y., and Kajii, Y.: A corresponding relationship between formaldehyde and missing• OH reactivity extrapolated in chamber studies using a mixture of nine VOCs and NOx, Atmospheric Environment, 121190, 2025.

Lou, S., Holland, F., Rohrer, F., Lu, K., Bohn, B., Brauers, T., Chang, C. C., Fuchs, H., Häseler, R., Kita, K., Kondo, Y., Li, X., Shao, M., Zeng, L., Wahner, A., Zhang, Y., Wang, W., and Hofzumahaus, A.: Atmospheric OH reactivities in the Pearl River Delta – China in summer 2006: measurement and model results, Atmos. Chem. Phys., 10, 11243–11260, https://doi.org/10.5194/acp-10-11243-2010, 2010.

Mao, J., Ren, X., Brune, W. H., Olson, J. R., Crawford, J. H., Fried, A., Huey, L. G., Cohen, R. C., Heikes, B., Singh, H. B., Blake, D. R., Sachse, G. W., Diskin, G. S., Hall, S. R., and Shetter, R. E.: Airborne measurement of OH reactivity during INTEX-B, Atmospheric Chemistry and Physics, 9, 163–173, https://doi.org/10.5194/acp-9-163-2009, 2009.

Mao, J., Ren, X., Chen, S., Brune, W. H., Chen, Z., Martinez, M., Harder, H., Lefer, B., Rappenglück, B., Flynn, J., and Leuchner, M.: Atmospheric oxidation capacity in the summer of Houston 2006: Comparison with summer measurements in other metropolitan studies, Atmospheric Environment, 44, 4107–4115, https://doi.org/10.1016/j.atmosenv.2009.01.013, 2010.

Morino, Y., Iijima, A., Chatani, S., Sato, K., Kumagai, K., Ikemori, F., Ramasamy, S., Fujitani, Y., Kimura, C., Tanabe, K., Sugata, S., Takami, A., Ohara, T., Tago, H., Saito, Y., Saito, S., and Hoshi, J.: Source apportionment of anthropogenic and biogenic organic aerosol over the Tokyo metropolitan area from forward and receptor models, Science of The Total Environment, 904, 166034, https://doi.org/10.1016/j.scitotenv.2023.166034, 2023.

Orlando, J. J. and Tyndall, G. S.: Laboratory studies of organic peroxy radical chemistry: An overview with emphasis on recent issues of atmospheric significance, Chemical Society Reviews, 41, 6294–6317, https://doi.org/10.1039/c2cs35166h, 2012.

Parker, A. E., Amedro, D., Schoemaecker, C., and Fittschen, C.: OH RADICAL REACTIVITY MEASUREMENTS BY FAGE, Environ. Eng. Manag. J., 10, 107–114, https://doi.org/10.30638/eemj.2011.015, 2011.

https://doi.org/10.5194/egusphere-2026-4769
Preprint. Discussion started: 14 September 2026

Ramasamy, S., Ida, A., Jones, C., Kato, S., Tsurumaru, H., Kishimoto, I., Kawasaki, S., Sadanaga, Y., Nakashima, Y., Nakayama, T., and others: Total OH reactivity measurement in a BVOC dominated temperate forest during a summer campaign, 2014, Atmospheric Environment, 131, 41–54, https://doi.org/10.1016/j.atmosenv.2016.01.039, 2016.

Ramasamy, S., Nagai, Y., Takeuchi, N., Yamasaki, S., Shoji, K., Ida, A., Jones, C., Tsurumaru, H., Suzuki, Y., Yoshino, A., Shimada, K., Nakashima, Y., Kato, S., Hatakeyama, S., Matsuda, K., and Kajii, Y.: Comprehensive measurements of atmospheric OH reactivity and trace species within a suburban forest near Tokyo during AQUAS-TAMA campaign, Atmospheric Environment, 184, 166–176, https://doi.org/10.1016/j.atmosenv.2018.04.035, 2018.

Ren, X., Van Duin, D., Cazorla, M., Chen, S., Mao, J., Zhang, L., Brune, W. H., Flynn, J. H., Grossberg, N., Lefer, B. L., Rappenglück, B., Wong, K. W., Tsai, C., Stutz, J., Dibb, J. E., Thomas Jobson, B., Luke, W. T., and Kelley, P.: Atmospheric oxidation chemistry and ozone production: Results from SHARP 2009 in Houston, Texas, JGR Atmospheres, 118, 5770–5780, https://doi.org/10.1002/jgrd.50342, 2013.

Sadanaga, Y., Yoshino, A., Watanabe, K., Yoshioka, A., Wakazono, Y., Kanaya, Y., and Kajii, Y.: Development of a measurement system of OH reactivity in the atmosphere by using a laser-induced pump and probe technique, Review of Scientific Instruments, 75, 2648–2655, https://doi.org/10.1063/1.1775311, 2004a.

Sadanaga, Y., Matsumoto, J., Sakurai, K. I., Isozaki, R., Kato, S., Nomaguchi, T., Bandow, H., and Kajii, Y.: Development of a measurement system of peroxy radicals using a chemical amplification/laser-induced fluorescence technique, Review of Scientific Instruments, 75, 864–872, https://doi.org/10.1063/1.1666985, 2004b.

Sadanaga, Y., Nojiri, R., Fukusaki, Y., Kousa, Y., Nakashima, Y., Kohno, N., Zhou, J., Li, J., Sakamoto, Y., Sato, K., Yoshino, A., Takami, A., Nakayama, T., Matsuoka, M., and Kajii, Y.: Direct evaluation of the ozone production regime in the Keihin Industrial Zone, Japan, Atmospheric Environment, 374, 121990, https://doi.org/10.1016/j.atmosenv.2026.121990, 2026.

Sakamoto, Y., Sadanaga, Y., Li, J., Matsuoka, K., Takemura, M., Fujii, T., Nakagawa, M., Kohno, N., Nakashima, Y., Sato, K., Nakayama, T., Kato, S., Takami, A., Yoshino, A., Murano, K., and Kajii, Y.: Relative and Absolute Sensitivity Analysis on Ozone Production in Tsukuba, a City in Japan, Environmental Science and Technology, 53, 13629–13635, https://doi.org/10.1021/acs.est.9b03542, 2019.

Sakamoto, Y., Egami, K., Li, J., Morino, Y., Nakashima, Y., Kato, S., Sato, K., Yoshino, A., Takami, A., Kohno, N., Sadanaga, Y., and Kajii, Y.: ROx budget analysis based on total OH reactivity and total ROx concentration measurements in Suburban Japan, Atmospheric Environment, 382, 122232, https://doi.org/10.1016/j.atmosenv.2026.122232, 2026.

Sato, K., Morino, Y., Sakamoto, Y., Li, J., Sadanaga, Y., Kajii, Y., and Imamura, T.: A chamber study on effects of aerosol particles upon tropospheric ozone production, Atmospheric Environment, 381, 122136, https://doi.org/10.1016/j.atmosenv.2026.122136, 2026.

Sinha, V., Williams, J., Crowley, J. N., and Lelieveld, J.: The Comparative Reactivity Method – a new tool to measure total OH Reactivity in ambient air, Atmos. Chem. Phys., 2008.

Sinha, V., Williams, J., Diesch, J. M., Drewnick, F., Martinez, M., Harder, H., Regelin, E., Kubistin, D., Bozem, H., Hosaynali-Beygi, Z., Fischer, H., Andrés-Hernández, M. D., Kartal, D., Adame, J. A., and Lelieveld, J.: Constraints on instantaneous ozone production rates and regimes during DOMINO derived using in-situ OH reactivity measurements, Atmospheric Chemistry and Physics, 12, 7269–7283, https://doi.org/10.5194/acp-12-7269-2012, 2012.

Tan, J., Zhang, Y., Ma, W., Yu, Q., Wang, Q., Fu, Q., Zhou, B., Chen, J., and Chen, L.: Evaluation and potential improvements of WRF/CMAQ in simulating multi-levels air pollution in megacity Shanghai, China, Stoch Environ Res Risk Assess, 31, 2513–2526, https://doi.org/10.1007/s00477-016-1342-3, 2017.

https://doi.org/10.5194/egusphere-2026-4769
Preprint. Discussion started: 14 September 2026

Tsai, C.-S., Huang, P.-C., Lai, H.-C., Lin, J. C., and Hung, H.-M.: Addressing underestimated carbon monoxide emissions in Taiwan using CMAQ and impacts on local ozone concentration, Atmospheric Environment: X, 26, 100325, https://doi.org/10.1016/j.aeaoa.2025.100325, 2025.

Wang, W., Qi, J., Zhou, J., Yuan, B., Peng, Y., Wang, S., Yang, S., Williams, J., Sinha, V., and Shao, M.: The improved comparative reactivity method (ICRM): measurements of OH reactivity under high-NO_x conditions in ambient air, Atmos. Meas. Tech., 14, 2285–2298, https://doi.org/10.5194/amt-14-2285-2021, 2021.

Wei, J., Li, Z., Wang, J., Li, C., Gupta, P., and Cribb, M.: Ground-level gaseous pollutants (NO_2 , SO_2 , and CO) in China: daily seamless mapping and spatiotemporal variations, Atmos. Chem. Phys., 23, 1511–1532, https://doi.org/10.5194/acp-23-1511-2023, 2023.

Whalley, L. K., Stone, D., Bandy, B., Dunmore, R., Hamilton, J. F., Hopkins, J., Lee, J. D., Lewis, A. C., and Heard, D. E.: Atmospheric OH reactivity in central London: Observations, model predictions and estimates of in situ ozone production, Atmospheric Chemistry and Physics, 16, 2109–2122, https://doi.org/10.5194/acp-16-2109-2016, 2016.

Yang, X.: A Review of the Direct Measurement of Total OH Reactivity: Ambient Air and Vehicular Emission, Sustainability, 15, 16246, https://doi.org/10.3390/su152316246, 2023.

Yang, Y., Shao, M., Wang, X., Nölscher, A. C., Kessel, S., Guenther, A., and Williams, J.: Towards a quantitative understanding of total OH reactivity: A review, Atmospheric Environment, 134, 147–161, https://doi.org/10.1016/j.atmosenv.2016.03.010, 2016.

Yoshino, A., Sadanaga, Y., Watanabe, K., Kato, S., Miyakawa, Y., Matsumoto, J., and Kajii, Y.: Measurement of total OH reactivity by laser-induced pump and probe technique-comprehensive observations in the urban atmosphere of Tokyo, Atmospheric Environment, 40, 7869–7881, https://doi.org/10.1016/j.atmosenv.2006.07.023, 2006.

Yoshino, A., Nakashima, Y., Miyazaki, K., Kato, S., Suthawaree, J., Shimo, N., Matsunaga, S., Chatani, S., Apel, E., Greenberg, J., Guenther, A., Ueno, H., Sasaki, H., Hoshi, J., Yokota, H., Ishii, K., and Yoshizumi Kajii: Air quality diagnosis from comprehensive observations of total OH reactivity and reactive trace species in urban central Tokyo, Atmospheric Environment, 49, 51–59, https://doi.org/10.1016/j.atmosenv.2011.12.029, 2012.

Zheng, B., Chevallier, F., Ciais, P., Yin, Y., Deeter, M. N., Worden, H. M., Wang, Y., Zhang, Q., and He, K.: Rapid decline in carbon monoxide emissions and export from East Asia between years 2005 and 2016, Environ. Res. Lett., 13, 044007, https://doi.org/10.1088/1748-9326/aab2b3, 2018.